Atmospheric Environment 239 (2020) 117738

Contents lists available at ScienceDirect

Atmospheric Environment

journal homepage: http://www.elsevier.com/locate/atmosenv

Assessment of dominating aerosol properties and their long-term trend in the Pan-Third Pole region: A study with 10-year multi-sensor measurements

Tianhe Wang [a], Yixuan Chen [a,b], Zewen Gan [a], Ying Han [a], Jiming Li [a], Jianping Huang [a,*]

[a] *Key Laboratory for Semi-Arid Climate Change of the Ministry of Education, Lanzhou University, Lanzhou, 730000, China*
[b] *Guizhou Meteorological Bureau, Guiyang, 550002, China*

HIGHLIGHTS

- Tibetan Plateau is the cleanest area of the Pan-Third Pole while mostly exposed to polluted air masses.
- The Pan-Third Pole region is dominated by absorbing aerosols such as dust, polluted dust and smoke.
- Vertical transport of aerosol is enhanced significantly along with the increase of topographic height.
- Trends of total aerosol loading are mainly influenced by those of dominating aerosol types.

ARTICLE INFO

Keywords:
The Pan-Third Pole
Dominating aerosol
Long-term trend
Active/passive satellite

ABSTRACT

The Pan-Third Pole (PTP), stretching from Eastern Asia to Middle-central Europe, has experienced unprecedented accelerated warming and even retreat of glaciers. Absorbing aerosols reduce snow and ice albedo and radiative forcing, consequently enhancing a great melting of snow cover and ice sheet in the PTP. Employing the 10-year (2007–2016) space-based active and passive measurements, this study investigated the distribution, optical properties and decadal trends for dominating aerosols at a seasonal scale in the PTP divided into six sub-regions. Results showed that the sub-regions of PTP were mainly dominated by dust, polluted dust and elevated smoke. The Taklimakan Desert (TD) and the Iranian Plateau (IP) were dominated by mineral dust, accounting for 96% and 86% of the total aerosol extinction while the Central Europe (CE), Indo-China (IC) and Anatolia Plateau (AP) were dominated by the mixture of the dominating aerosol types. The mean aerosol extinction coefficient (MAEC) showed an obvious variability depending on the sub-regions and a tendency of decreasing with an increase in the topographic height. The strongest extinction layer (>0.1 km^{-1}) mainly occurred below 4 km and the weak extinction layers (>0.001 km^{-1}) were mainly distributed between 5 km and 8 km, indicating pronounced vertical transport in the region. The decadal trends of columnar aerosol optical depth (AOD) showed a relation with the contributions of the dominating aerosol types. For example, significant upward or downward trends of total aerosol loading in the IC region were driven by elevated smoke while the AOD trends of total aerosol loading for the CE, the AP and the IP were driven by the dominating aerosol types. The Tibetan Plateau (TP), the cleanest region in the PTP, has been regularly exposed to polluted air masses with significant amounts of absorbing aerosols. Therefore, understanding the dominating aerosol types, properties and decadal trends in the PTP region will contribute considerably to assessing their effects on radiative forcing, climate change, and even snowmelt and glacier retreat.

1. Introduction

Atmospheric aerosols are key factors that extensively play a vital role in climate change at regional and global scales, primarily due to their significant direct and indirect effects on atmospheric systems (Garrett and Zhao, 2006; Huang et al., 2006a, 2006b, 2014; Li et al., 2011, 2016b, 2019; Rosenfeld et al., 2008; Zhao and Garrett, 2015). For instance, atmospheric aerosols directly influence on absorbing and scattering solar shortwave and terrestrial longwave radiations, resulting in climate change driven by the alterations of the radiative and energy

* Corresponding author.
E-mail address: hjp@lzu.edu.cn (J. Huang).

https://doi.org/10.1016/j.atmosenv.2020.117738
Received 29 January 2020; Received in revised form 24 May 2020; Accepted 23 June 2020
Available online 7 July 2020

balance of the earth (Che et al., 2019b; Yang et al., 2016, 2018). Absorbing aerosols, e.g., black carbon (BC), organic carbon (OC) and mineral dust, could especially contribute to large diabatic heating in the atmosphere, which may induce not only enhanced cloud evaporation (Ackerman et al., 2000; Huang et al., 2006a; Koren et al., 2004; Yan and Wang, 2020) but also reducing snow and ice albedo, resulting in a great melting potential on glaciers (Xu et al., 2009). In this regard, aerosols may indirectly affect alterations in global surface temperature, land surface process, climate and hydrological cycle, and the ecosystems (Ramanathan et al., 2001, 2007). Many studies have also concluded that aerosols have detrimental impacts on air quality (Fan et al., 2020), visibility (Deng et al., 2011) and human health (Davidson et al., 2005). Therefore, it is crucial to profoundly understand the physical, optical and chemical properties of aerosols at different spatial-temporal scales.

The Pan-Third Pole region (PTP), populating more than 3 billion people, is the core of the "The Belt and Road" initiative proposed and advanced by China (Yao et al., 2017). Since the implementation of the initiative, the environmental changes of the PTP region have caught worldwide attention more and more as it includes the greatest area of snow cover and ice sheet in the world except for the polar region. Freshwater for the surroundings is sourced from meltwater discharge at the high mountain regions. Under the global warming, the PTP region, especially for the Tibetan Plateau (TP), has experienced rapid accelerated warming over the last decades (Huang et al., 2012) at a rate that far exceeds those for the same latitudinal areas during the same period, especially in winter (Yang et al., 2014). This warming trend is considered to be the main source for the retreat of glaciers and even an increase in lake levels over TP and river runoff in the surrounding areas (Yao et al., 2004; Zhang et al., 2011), which may have impacts on the regional and global hydrologic cycle (Barnett et al., 2005). In addition, light-absorbing impurities from the deposition of atmospheric absorbing aerosols, such as BC, OC and mineral dust, are all known to exert a great melting potential on these glaciers through reducing snow and ice albedo and radiative forcing, which has been verified through a number of field sampling analysis in snow and glaciers over both TP and surroundings (Gautam et al., 2013; Jacobi et al., 2015; Li et al., 2016a; Luthi et al., 2015) and numerical simulations (Lau et al., 2010; Xu et al., 2016; Yasunari et al., 2015).

In recent years, desertification and human activities, e.g., overgrazing, intensive biomass burning, and tourism development, have aggravated the ecological environment deterioration over the PTP region. The anthropogenic aerosol emission and special dust processes (Wang et al., 2018b) have been focused as the biggest threat to the environment and human health over the PTP region (Pokharel et al., 2019; Zhao et al., 2020). Satellite-based measurements in the work of van Donkelaar et al. (2010) showed that the airborne fine particulate matter with diameter less than 2.5 μm ($PM_{2.5}$) covered from central Asia to eastern Asia along the whole PTP region. In particular, the regional population of 38–50% is affected by the particulate matter exceeding the World Health Organization Air Quality guideline and $PM_{2.5}$ Interim Target-1 (35 μg/m^3 annual average). The longer lifetimes of these aerosols in free troposphere allow a higher opportunity to be transported farther depending on a weather system, i.e., the wider spatial coverage of these aerosols in effect from the sources. Despite being a remote and sparsely populated area, TP has been regularly exposed to polluted air masses with significant amounts of absorbing aerosols including BC, OC and dust (Luthi et al., 2015; Zhao et al., 2020). The potential sources of the deposited absorbing aerosol pollutants over the glaciers in the Karakoram-Himalayan region of northern Pakistan were identified in central, south, and west Asia (Gul et al., 2018). Hofer et al. (2017) detected dust and pollutants sourced from the Middle East, Northern Africa and Central Asia during the Central Asian Dust Experiment (CADEX) in Dushanbe, Tajikistan. Many studies also examined the enhanced trans-Himalaya pollutants transport mainly driven by intensive biomass burning emissions to the TP based on various proxies extracted from glaciers such as short-lived reactive aromatics (Zhang et al., 2017), carbon isotope (Li et al., 2016a), organic acid (Cong et al., 2015), levoglucosan records (You et al., 2016) and so on.

Identifying aerosol types, spatial-temporal distribution and long-term trends at global or regional scales is crucial to comprehensively understand the aerosol transport and removal processes, emission properties, vertical uplifts, and even aerosol-induced climate change. The columnar distribution and trends were usually evaluated using columnar aerosol optical depth (AOD) from surface-based Aerosol Robotic Network (AERONET) (Li et al., 2014) and passive satellite sensors such as Multi-angle Imaging Spectroradiometer (MISR) (Mehta et al., 2016), Ozone Monitoring Instrument (OMI) (Chimot et al., 2017), Moderate Resolution Imaging Spectroradiometer (MODIS) (Luo et al., 2014), Visible Infrared Imaging Radiometer Suite (VIIRS) (Yang et al., 2019) and others (Hsu et al., 2012; Prospero et al., 2002) or multi-sensor combination(Alfaro-Contreras et al., 2017; Wang and Huang, 2009). The vertical distributions were usually measured by the active Cloud-Aerosol Lidar with Orthogonal Polarization (CALIOP) onboard the Cloud-Aerosol Lidar and Infrared Pathfinder Satellite Observations (CALIPSO) (Huang et al., 2015b; Winker et al., 2013). However, there are few comprehensive studies on the climatology of aerosol over the PTP, especially focusing on the dominating aerosol types. This study, therefore, aims to investigate the climatology of columnar and vertical distribution for optical properties, the dominating aerosol types, and their temporal trends over the PTP region by combining aerosol products from A-Train constellation. In particular, understanding the characteristics of absorbing aerosols is very important with regard to assessing their effects on the retreat of glaciers, increase of lake levels, river runoff, and the regional and even global hydrologic cycle.

The paper is organized as follows: Section 2 briefly describes aerosol data products deployed in this study. The definition and climatic features within the study domain are depicted in Section 3. Section 4 discusses the columnar and vertical distribution of the dominating aerosol types in detail and quantifies mean aerosol extinction coefficients (MAEC) over the different sub-regions of PTP. The deseasonalized linear decadal trends of AOD for total and dominating aerosol types are presented in Section 4. Finally, the main conclusions are presented in Section 5.

2. Satellite-based aerosol products

2.1. CALIPSO vertical feature mask (VFM) and aerosol profile products

CALIPSO has been launched in June 2006 to provide continuous measurements for aerosols backscatter, extinction and depolarization profiles at a global scale during both day and night (Winker et al., 2009). This study employed not only the newest version 4 level 2 VFM that provides feature classification from ground to stratosphere but also the level 3 monthly aerosol profile (CL3AP) of CALIPSO satellite during a 10-year period from 2007 to 2016. Aerosol types in the troposphere are categorized into seven subtypes (e.g., dust, polluted dust, clean continental, polluted continental/smoke, elevated smoke, clean marine and dusty marine) by the Scene Classification Algorithm (Omar et al., 2009) that uses the integrated attenuated backscatter and the particulate depolarization ratio measurements, surface type, layer top and base altitudes to identify the aerosol subtypes. An advantage of the depolarization technology is to allow for a separation of mineral dust (Liu et al., 2004) and smoke (Sun et al., 2013) from other types of aerosols. The CL3AP reports monthly mean profiles of aerosol optical properties on a uniform spatial grid at horizontal resolution of 2° × 5° and vertical resolution of 60 m (from - 0.5 km to 12 km a.m.s.l.). All parameters are derived from the level 2 5-km aerosol profile products that are quality controlled prior to aggregating onto each grid and averaging (Winker et al., 2013). In addition, the CL3AP provides the aerosol classification at each grid cell. Each aerosol subtype has a lidar ratio which is preassigned for the aerosol extinction retrieval. The assumption of lidar ratio and subtype misclassification are the crucial factors that affect the uncertainty in the aerosol extinction retrieval (Yang et al., 2019; Yu et al., 2010). Neverthless, previous studies have demonstrated that the CL3AP provides representative and realistic data for the aerosol extinction values, larger than about 0.001 km^{-1} in most cases (Winker et al., 2013), by comparing the accuracy of CL3AP with other satellite sensors and ground-based measurements (Kim et al., 2013; Mona et al., 2009; Papagiannopoulos et al., 2016; Schuster et al., 2012). Therefore, the nighttime aerosol layers feature and optical properties with the cloud-aerosol-discrimination (CAD) scores between -70 and -100 were employed in this study to avoid the low-confidence classification and extinction retrieval of layer features.

2.2. MODIS and OMI columnar AOD

MODIS plays a key role in observing global environmental and climate changes by an instrument aboard NASA's Terra and Aqua satellites (Savtchenko et al., 2004). It has been acquiring an extreme volume of data in 36 spectral bands between 0.4 and 14.4 μm for land, atmosphere, ocean and cryosphere since March 2000 for Terra and July 2002 for Aqua. The level 2 MODIS collection-6 aerosol products over land and ocean are based on two algorithms: 1) enhanced deep blue (Hsu et al., 2013) and 2) dark target (Levy et al., 2013). These two algorithms have been developed to work over bright surfaces and mainly vegetated or water surfaces, respectively. Many studies evaluated the performance of collection-6 AOD based on ground observations (Sayer et al., 2014; Tao et al., 2015). OMI is a nadir-viewing spectrometer onboard the NASA EOS Aura spacecraft that observes the top of atmosphere solar backscatter radiation in the ultraviolet (UV) and visible spectrum (270–500 nm) (Torres et al., 2007). OMI has been originally designed to monitor global ozone and other atmospheric parameters related to ozone chemistry and climate. Furthermore, it provides valuable aerosol information especially for detecting elevated layers of absorbing aerosols such as biomass burning and dust plumes. Employing the columnar AOD from MODIS/Aqua collection-6 Level 3 atmosphere monthly global product (MYD08_M3) and the OMI near-UV retrieval algorithm products (OMAERUVd) at $1^\circ \times 1^\circ$ spatial resolution, this study investigated the columnar AOD distributions driven by different retrieval algorithms over the PTP region.

3. Climatic features of the PTP and study domain

The PTP stretches from Eastern Asian to Middle-central Europe (CE), delineated with a red-colored polygon in Fig. 1a, including high-elevation mountain regions (e.g., TP and Tianshan Mountains in China), Pamirs across Tajikistan, China and Afghanistan, the Hindu Kush in between Afghanistan and Pakistan, the Iranian Plateau (IP), the Caucasus in between the Black Sea and the Caspian Sea, the Anatolia Plateau (AP), and the Carpathian Mountains across Central and Eastern Europe. As the PTP possesses various socioeconomic features, global biodiversity hot-spots, and rich natural resources, it plays a crucial role in human existence environment and sustainable development and acts as environmental and ecological barrier for China, Asia, and even for the Northern Hemisphere (Kang et al., 2010; Yao et al., 2017). Besides, the PTP consists of distinct climatic zones, as shown by the annual mean

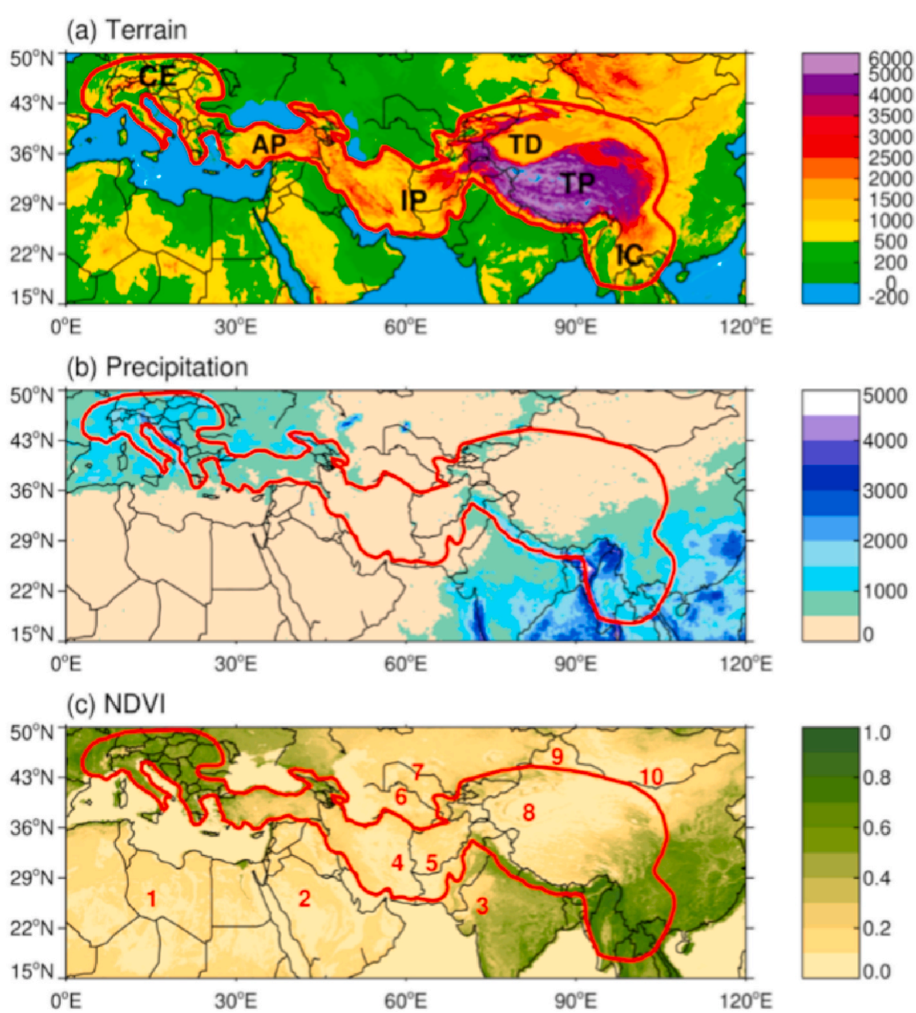

Fig. 1. The spatial distribution of (a) terrain (unit: m), (b) annual mean precipitation rate (unit: mm/year) from TRMM, and (c) NDVI from MODIS/Terra over the PTP and surroundings. The core region of PTP is delineated with a red-colored polygon, including six sub-regions labeled with the captial letters of CE, AP, IP, TD, TP and IC. The surrounding dust sources are presented in red numbers, which are (1) the Sahara desert, (2) the Arabian desert, (3) the Thar desert, (4) the Dasht-e Lut desert, (5) the Rigestan desert, (6) the Karakum desert, (7) the Kyzylkum desert, (8) the Taklimakan desert, (9) the Gurbantunggut desert, and (10) the Gobi desert, respectively.

precipitation rate from Tropical Rainfall Measurement Mission (TRMM) and Normalized Difference Vegetation Index (NDVI) from MODIS/Terra in Fig. 1b and c, respectively. The maximum of annual mean precipitation mainly appears on the southern slope of TP due to the monsoon systems dominated by the interactions of large-scale atmospheric circulations including the mid-latitude westerlies, the East Asian monsoon and the Indian monsoon (Wu et al., 2015; Yao et al., 2017).

In addition, there is a large portion of arid and semi-arid regions (Huang et al., 2015a), currently facing accelerated expansion (Huang et al., 2015c) and potential treat (Huang et al., 2017) under the background of global warming. The whole PTP is cut off by the global dust belt, which reaches from the Sahara over the Arabian deserts to the Taklimakan Desert (TD) and the Gobi Desert (GD). The PTP contains global dust sources presented in red numbers in Fig. 1c such as the TD, the Iranian Dasht-e Lut desert, and the Rigestan desert in Afghanistan, and also adjacent to the Sahara and Arabian deserts, the Kyzylkum and Karakum deserts. Atmospheric mineral dust can be transported over tens of thousands of kilometers away from the arid or semi-arid source regions. For instance, Sahara dust can be transported eastward to the Middle East and East Asia (Kabatas et al., 2014; Tanaka et al., 2005), northward to Europe (Israelevich et al., 2012), and westward to America (Mckendry et al., 2007). The TD and GD in China and the Thar desert on the Indian Subcontinent are also abundant dust sources, subordinate only to North Africa and the Arabian Peninsula (Liu et al., 2008). The observations from CALIPSO demonstrated that dust events occurred over the Taklimakan all year round and dust aerosols may be accumulated over the northern slope of the TP (Huang et al., 2007), northward to the north pole (Huang et al., 2015d) and eastward to downstream (Huang et al., 2008; Uno et al., 2009). Most severe $PM_{2.5}$ pollutions from central Asia to eastern Asia along the whole PTP region were monitored by satellite measurements (van Donkelaar et al., 2010). With regard to the climatic feature and the potential natural and anthropogenic aerosol sources, therefore, the PTP was divided into six sub-regions in this study as follows: (1) CE (47–51°N, 15–30°E), (2) AP (37–41°N, 30–45°E), (3) IP (31–35°N, 45–75°E), (4) TD (37–39°N, 75–85°E), (5) TP (29–37°N, 85–95°E), and (6) Indo-China (IC) (17–29°N, 95–105°E).

4. Results analysis and discussion

4.1. Columnar AODs distribution

Fig. 2 shows the spatial distributions of decadal mean columnar AODs driven by CALIOP, MODIS, and OMI over the PTP for spring (MAM), summer (JJA), autumn (SON) and winter (DJF). High magnitudes of AODs were obviously observed in the Arabian Peninsula, Tarim Basin, Indian subcontinent, IC, and the eastern of China throughout the year. In the nearby PTP, the maximum of AODs occurred over the Arabian Peninsula and the adjacent Arabian Sea in summer, which may be caused by more active dust outbreaks in this region. Dust aerosols generated in this source region for all seasons may be transported to the Persian Gulf and the Arabian Sea (Badarinath et al., 2010) and northward to Central Asia (Hofer et al., 2017), and subsequently inducing significant effects on the Asian summer monsoon (Jin and Wang, 2018). While the seasonal difference of columnar AOD over the Arabian Sea is significant (refer to Fig. 2), a larger difference in the extent and magnitude of AODs between three sensors was also found. The second maximum of AODs occurred in the Sichuan basin and eastern China for all seasons, where industrial expansion, urbanization, and rapid economic developments have been actively conducted (Che et al., 2015; Fan et al., 2020; Zhang et al., 2019; Zhang and Cao, 2015). While the pattern of AODs distribution for CALIOP is similar to that of MODIS, it is highly different from the ones for OMI, especially in SON and DJF. In addition, a relatively higher AOD for all seasons was found in the Indian subcontinent in which arid Pakistan and northwestern India and extensive desert regions (e.g., the Thar desert) are located. The spatial distributions of AODs driven by CALIOP and MODIS were similar to each other except for that high AODs were found along the southern edge of the TP for MODIS. However, it is noteworthy that there are prominent

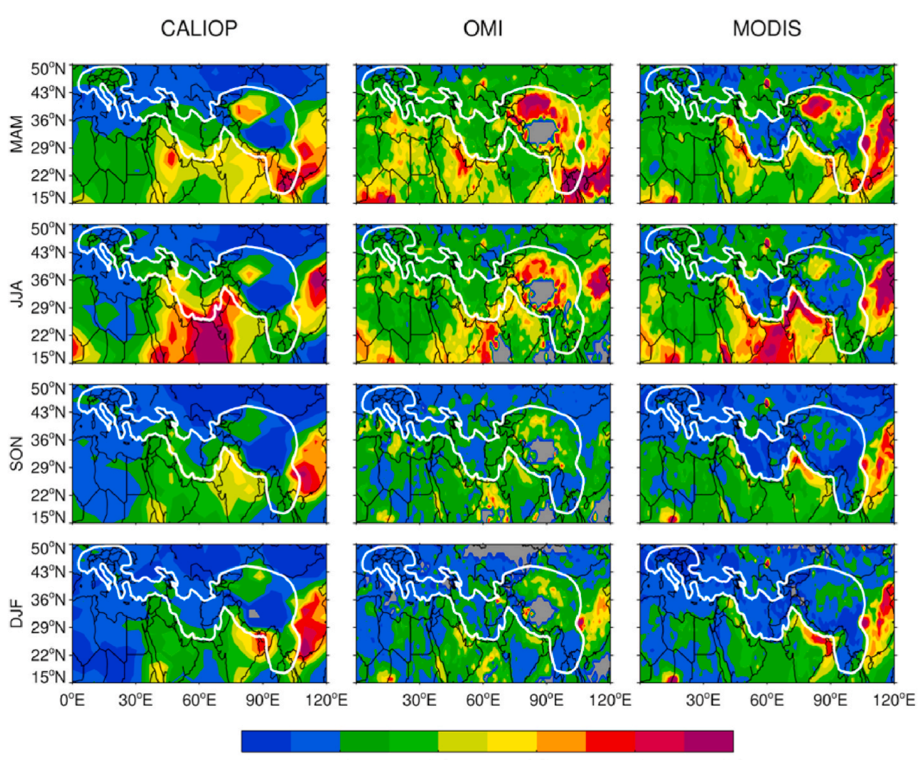

Fig. 2. Comparizon of decadal mean columnar AODs distribution from CALIOP at 532 nm (left), OMI at 500 nm (middle), MODIS/Aqua at 550 nm (right) over the PTP and surroundings. The core region of PTP is delineated with white-colored polygon. The grey areas represent no retrievals in these regions.

differences in the columnar AODs between active CALIOP and passive MODIS and OMI in the north part of the Iranian Plateau that includes the two great deserts of Central Asia, the Kyzylkum and Karakum deserts. Although CALIPSO retrieves AOD based on the aerosol extinction vertical profile, the signal-to-noise ratio is often too low to accurately detect the weak aerosol layers from the aerosol extinction vertical profile. In other words, highly diffuse and tenuous scattering aerosol layers below a CALIPSO detection threshold might be ignored in the AOD retrieval processes. This may cause the lower AODs obtained from CALIPSO than those from MODIS and OMI. In addition, the lower AODs of CALIPSO may be induced by the CALIOP's 16-day repeating cycle that possibly misses important outbreaks of dust events in this region.

The columnar AOD distributions over the whole PTP have distinct regional and seasonal variability due to the local emissions and the transport of natural and anthropogenic aerosols from the nearby PTP region. Table 1 shows the decadal mean and standard deviation of the columnar AODs driven by different sensors at the six sub-regions for different seasons. The TD has the largest seasonal variation among the six sub-regions, the highest (lowest) value was 0.68 (0.22) from CALIOP, 0.82 (0.31) from OMI, and 0.80 (0.19) from MODIS during MAM (DJF) respectively. The largest AOD was observed in IC, 0.95 from OMI during MAM while larger standard deviations were observed in IC, indicating the complex aerosol composition in IC (will be discussed at the following section). On the contrary, the TP showed a lower columnar AOD (i.e., the cleanest area) in the PTP region, the lowest columnar AOD from CALIOP, no AOD retrieval from OMI, and a larger AOD from MODIS close to the AP, IP and CE sub-regions. The results showed that AODs varied with sensor types and the differences in instruments, calibration, retrieval algorithms, sampling resolution and so on. Overall, however, the composite results suggested in this study may provide useful information further to understand the spatial distribution of aerosols in the PTP region.

4.2. The dominating aerosol types

Identifying the optical properties, classification, and vertical structure of aerosols, usually being detected by passive satellite measurements (Penning de Vries et al., 2015), is still a challenging task due to the broadband effect of aerosols on the measured spectra and the influences of surface and cloud reflection. To date, the CALIPSO-based aerosol classification and vertical structure are the most comprehensive and accurate aerosol products derived from an active depolarized detecting technique. In order to fully understand the dominating aerosol types over the PTP, furthermore, this study investigated the seasonal occurrence frequency (OF) of seven aerosol types from the CALIPSO satellite in horizontal and vertical directions.

Table 1
The mean and standard deviation (shown in bracket) of columnar AODs over the sub-regions of PTP during MAM, JJA, SON and DJF season, respectively.

Satellite	Season	Sub-regions of the PTP					
		CE	AP	IP	TD	TP	IC
CALIPSO	MAM	0.23 (0.02)	0.25 (0.07)	0.29 (0.07)	0.68 (0.01)	0.02 (0.007)	0.68 (0.25)
	JJA	0.17 (0.02)	0.35 (0.11)	0.38 (0.07)	0.66 (0.01)	0.03 (0.009)	0.30 (0.06)
	SON	0.17 (0.01)	0.26 (0.12)	0.19 (0.03)	0.26 (0.02)	0.006 (0.003)	0.40 (0.11)
	DJF	0.18 (0.01)	0.18 (0.05)	0.15 (0.02)	0.22 (0.01)	0.003 (0.004)	0.43 (0.15)
OMI	MAM	0.20 (0.02)	0.33 (0.06)	0.31 (0.06)	0.82 (0.06)	/	0.95 (0.40)
	JJA	0.22 (0.01)	0.29 (0.07)	0.30 (0.06)	0.69 (0.05)	/	0.33 (0.09)
	SON	0.12 (0.01)	0.22 (0.04)	0.21 (0.05)	0.38 (0.05)	/	0.19 (0.03)
	DJF	0.14 (0.02)	0.17 (0.04)	0.20 (0.05)	0.31 (0.05)	/	0.16 (0.03)
MODIS	MAM	0.21 (0.02)	0.22 (0.04)	0.17 (0.06)	0.80 (0.04)	0.28 (0.13)	0.52 (0.17)
	JJA	0.24 (0.01)	0.17 (0.05)	0.18 (0.12)	0.49 (0.07)	0.16 (0.06)	0.29 (0.07)
	SON	0.12 (0.02)	0.13 (0.03)	0.12 (0.06)	0.20 (0.02)	0.13 (0.07)	0.26 (0.06)
	DJF	0.08 (0.04)	0.14 (0.02)	0.13 (0.04)	0.19 (0.02)	0.15 (0.08)	0.21 (0.08)

4.2.1. Horizontal distribution

Fig. 3 shows the seasonal OF spatial maps for the selected seven aerosol types, i.e., (a) dust, (b) polluted dust, (c) elevated smoke, (d) polluted continental/smoke, (e) clean continental, (f) clean marine, and (g) dusty marine, where the OF for each aerosol type is defined as the ratio of the number of profiles of an aerosol type with high confidence to the total samples from surface to 10 km at each $2^\circ \times 2^\circ$ grid for each season. It is prominent that the natural dust is the most prevailing aerosol type for all seasons over the spatial domain in the maps (refer to Fig. 3a). The horizontal distribution of dust is well consistent with the global dust belt while showing a greater extent and significant seasonal variation. During MAM and JJA, the dust aerosols above 80% chances were observed in source and transport regions such as the Sahara desert, the Arabian Peninsula, the IP, the TD, and the Arabian Sea, which is consistent with the previous studies that employed different sensors (Luo et al., 2015; Prospero et al., 2002; Rashki et al., 2014; Wang et al., 2018a). However, the dust aerosol is rarely observed in the CE and IC sub-region for all seasons.

Polluted dust, a mixture of dust and anthropogenic pollutants such as biomass burning aerosols, can be frequently found around the regions of strong sources (Omar et al., 2009). Over the nearby PTP and PTP regions, the polluted dust is the second dominating aerosol type, frequently occurring in the regions where the dust aerosol occurred as shown in Fig. 3b. The hot-spots (i.e., OF > 50%) for the polluted dust are mainly located at the eastern and northern parts of Africa except for MAM, the Indian subcontinent except for JJA, the Arabian Peninsula in DJF, Central Asia close to the Karakum and Kyzylkum Deserts in JJA and SON, and eastern China in all seasons.

Fig. 3c-e exhibit the OF spatial maps for elevated smoke, polluted continental/smoke, and clean continental aerosol types, respectively, which shows a similar distribution pattern at different degrees of magnitudes. Elevated smoke is defined as an elevated non-depolarizing aerosol that is injected above the planetary boundary layer (PBL) due to combustion buoyancy. However, polluted continental/smoke represents polluted continental aerosol derived from anthropogenic pollutants within the PBL, which is difficult to separate from biomass burning smoke. These three aerosol types mainly occurred in CE for all seasons, in eastern China for JJA and SON, and the Indian subcontinent and the IC for SON and DJF, mainly induced by agricultural fires over Europe (Amiridis et al., 2010), crop straw field burning in eastern China (Cao et al., 2008), and a high rate of usage of biofuels and coal in India and the IC (Menon et al., 2002), respectively.

As marine aerosols are only defined above the surface of ocean, clean marine and dusty marine can be observed throughout the year in the oceanic areas around the PTP region such as the Mediterranean, the Black Sea, the Arabian Sea, the Bay of Bengal and South China Sea as shown in Fig. 3f and g. The high frequency of dusty marine in the Bay of Bengal and the Arabian Sea throughout the year is closely linked to the frequent occurrence of the dust and the polluted dust driven from the Middle East and the India subcontinent.

Overall, this study found that dust, polluted dust, elevated smoke and polluted continental/smoke are the major aerosol types dominating in different sub-regions seasonally within the PTP. It is noteworthy that the dominant aerosol types are typical absorbing aerosols that undoubtedly have crucial impacts on radiation and energy balance, water cycle, and climate change in the whole PTP region.

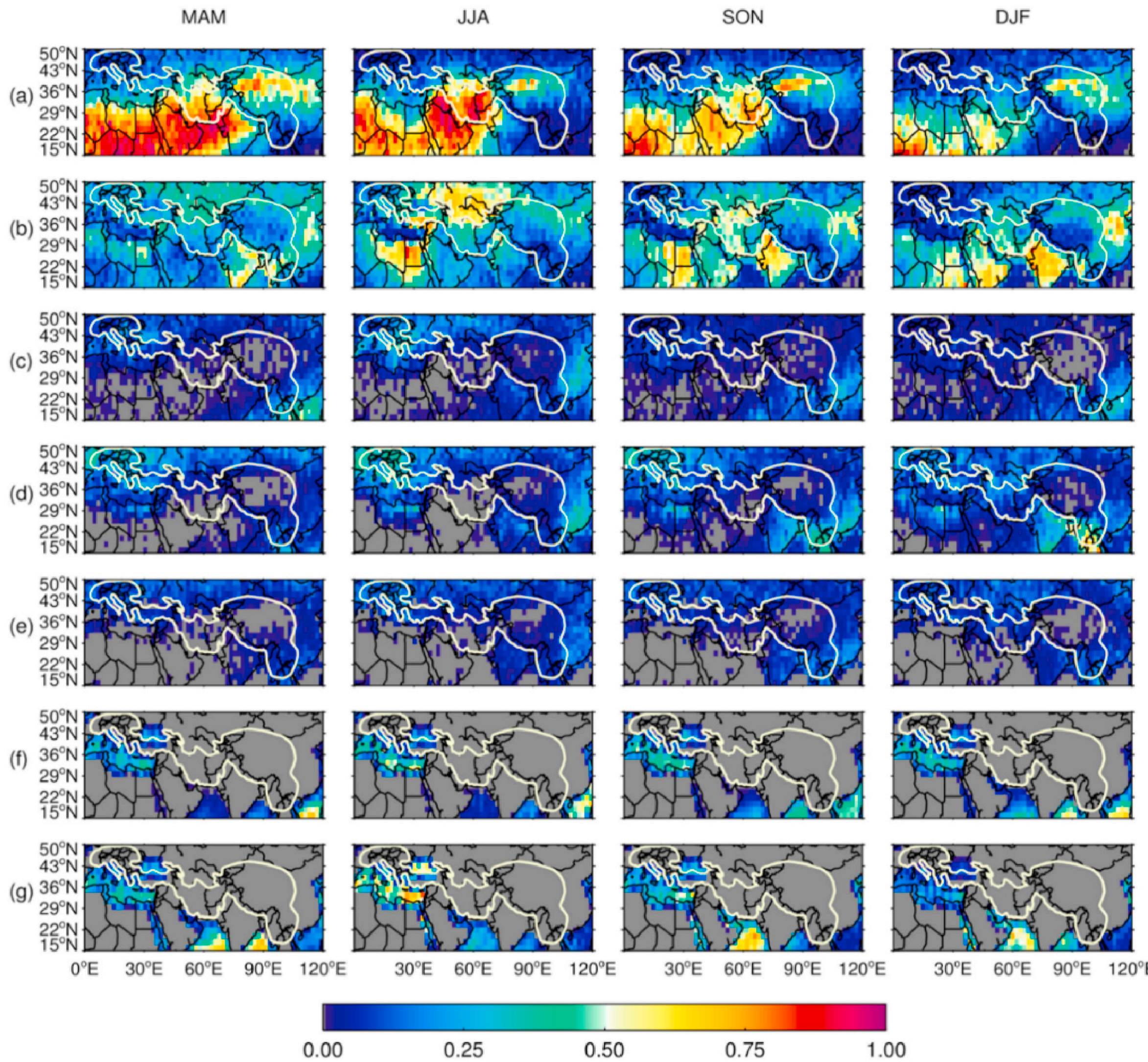

Fig. 3. Seasonal OF maps for seven aerosol types defined by CALIOP products over the PTP region from surface to 10 km (a.m.s.l): (a) dust, (b) polluted dust, (c) elevated smoke, (d) polluted continental/smoke, (e) clean continental, (f) clean marine, and (g) dusty marine. The core region of PTP is delineated with white-colored polygon.

4.2.2. Vertical distribution

This study also investigated the vertical-resolved aerosol OF, the ratio of an aerosol subtype in samples to the total samples at each given altitude level, to illustrate the contributions of the dominating aerosol types in the vertical aerosol profiles over six sub-regions in the PTP. Fig. 4 shows the seasonal vertical OF profile for the dominating aerosols identified by the horizontal distribution assessment over the six sub-regions. Interestingly, it is prominent that each sub-region is dominated by single or multiple aerosol types.

As in the horizontal distribution, dust is also the most abundant aerosol type of the IP and the TD sub-regions as shown in Fig. 4c and d. In addition, a strong vertical transport of the dust particles was found at higher altitudes, especially for TD in MAM exceeding 10 km a.m.s.l., due to the unique topography and northeasterly winds associated with certain synoptic conditions (Ge et al., 2014). The maximal OF (47% in MAM, 45% in JJA, 60% in SON, and 38% in DJF) appeared near the ground level in the TD and gradually decreases with the increase of height. However, the vertical OF profile in the IP showed a wave pattern corresponding to the height at different levels of the maximum seasonal values, for instance, 58% in MAM and 65% in JJA at the heights of 3.0 and 2.8 km a.m.s.l., respectively, which are much larger than those in the TD. It is closely related to more dust aerosol prominently transported from the nearby Sahara, the Arabian, and the Thar desert (Bayat et al., 2011; Léon and Legrand, 2003). On the contrary, dust over the TD is mostly sourced from local emissions.

Contrary to the IP and TD, the AP is dominated by the polluted dust with a high OF between the ground and 6 km a.m.s.l. at different levels of seasonal vertical transport as shown in Fig. 4b. The maximum OF (52%) occurred at 2.2 km a.m.s.l. in JJA, followed by SON and MAM. These results indicate that the frequent transport of dust from Sahara and Middle East, and significant industrial and anthropogenic pollutants from industrialized and populated regions (such as Turkey, Spain, France and Italy), are contributing to the vertical aerosol profiles in the AP, as confirmed by combining the satellite observation and Real-time Air Quality Modeling System (Kabatas et al., 2014) and long-term observation from AERONET (Tutsak and Kocak, 2019). In addition, dust from Sahara to the eastern Mediterranean occurs predominantly during the spring and is commonly associated with the eastward passage of a frontal low-pressure system, whilst dust from sources in the Middle East is more typically transported to the eastern Mediterranean in the autumn. In contrast, dust transport from Sahara to the western and central Mediterranean occurs mainly during the summer (Kocak et al., 2012; Kubilay et al., 2000).

The CE and IC show more complicated aerosol vertical distributions

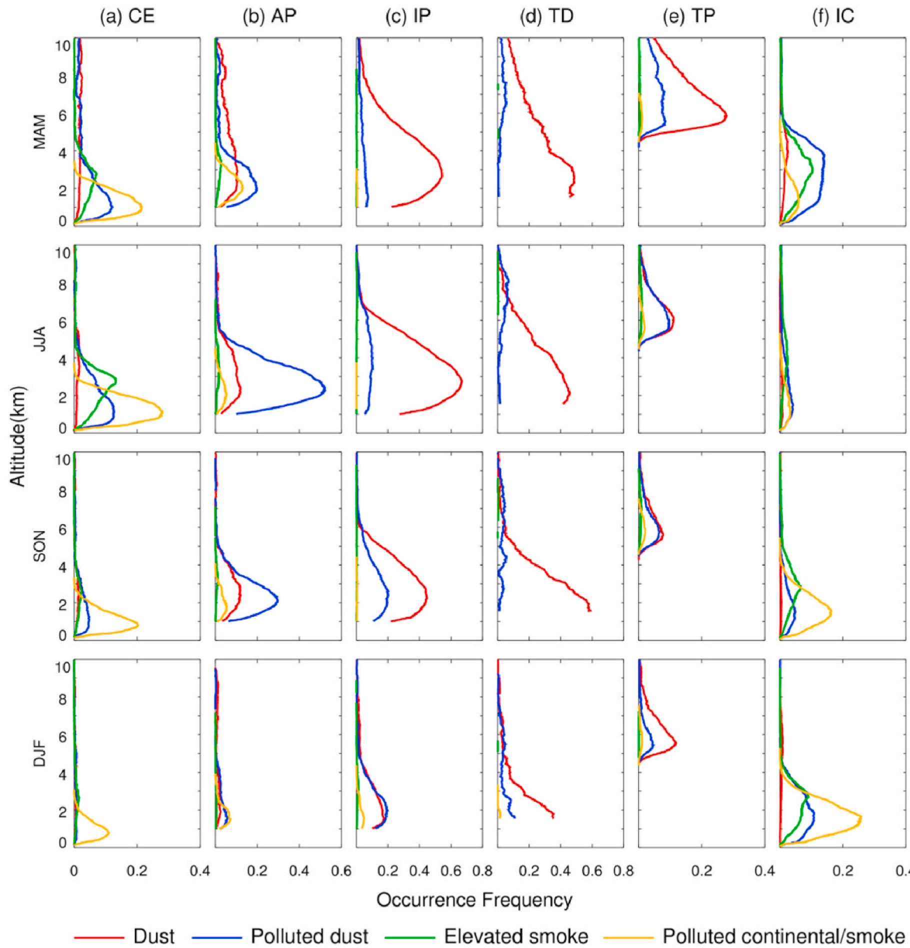

Fig. 4. Seasonal and vertical resolved OF for the dominating aerosols over the six sub-regions of (a) CE, (b) AP, (c) IP, (d) TD, (e) TP, and (f) IC from surface to 10 km (a.m.s.l) derived from CALIOP measurements.

than other sub-regions (refer to Fig. 4a and f, respectively). The polluted continental/smoke is dominating the vertical aerosol profiles in the CE for all seasons while only SON and DJF in the IC. As the polluted continental/smoke mainly occurred in the PBL, it is difficult to distinguish smoke and continental aerosol. Smoke mainly caused by biomass burning (e.g., agricultural fires, crop straw field burning, and high rates of usage of biofuels) can be lofted to higher altitudes due to the large heat-induced atmospheric instability. The occurrence of elevated smoke, which is injected from the PBL to higher altitudes, indicates that there must be a proportion of smoke trapped in the PBL and subsequently contributing to the polluted continental/smoke aerosols within the PBL. The correlation between the elevated smoke and the polluted continental/smoke aerosols is prominent in the CE during MAM and JJA and in the IC during MAM, SON and DJF. Although there are few local dust emissions over the IC as shown in Fig. 3a, the mixture of dust transported from the India subcontinent and smoke emitted from local industrial pollutants and anthropogenic activities may cause a higher OF of polluted dust during MAM and DJF.

Although the TP showed the smallest columnar AOD in the PTP (refer to Fig. 2), it is worth noting that during the MAM season, higher dust OF (30%) than other seasons was observed at about 6 km a.m.s.l., as shown in Fig. 4e. A new algorithm developed by Luo et al. (2015) enhanced the ability to detect weaker dust layers in weak source regions and the upper troposphere. In contrast, the light-absorbing impurities in snow and glaciers, such as organic carbon (OC), black carbon (BC) and mineral dust, have been verified by many field sampling analysis (Gautam et al., 2013; Jacobi et al., 2015; Li et al., 2016a; Luthi et al., 2015). Despite the vertical OF for the elevated smoke was much less than those for the dust and the polluted dust, the extinction contribution and significant increasing trend need to be considered as discussed in section 4.3 and 4.4. Thus, these results indicate that the TP has been regularly exposed to polluted air masses at a significant level of absorbing aerosols (Zhao et al., 2020).

4.3. Vertical distribution of mean aerosol extinction coefficient (MAEC)

To better understand the difference of MAEC and vertical transport of the dominating aerosols, the decadal means of MAEC for the six sub-regions were compared along longitudinal and latitudinal directions, as shown in Fig. 5 and Fig. 6, respectively. For simplicity, this study defined the altitudes corresponding to the aerosol layer top (>0.0001 km^{-1}), low extinction (LE, >0.001 km^{-1}), middle extinction (ME, >0.01 km^{-1}) and strong extinction (SE, >0.1 km^{-1}) layers as depicted in the figures. It should be specially explained that the altitudes of aerosol layers within the classified extinction levels are calculated as moving averages of three vertical resolution bins to avoid abrupt changes. In addition, the decadal means of the columnar AODs and the relative contributions of the dominating aerosols observed by CALIOP for the six sub-regions were calculated to quantify the extinction contribution of the dominating aerosol types as shown in Table 2.

Fig. 5 shows the longitudinal variation of decadal MAEC for All-aerosol and the dominating aerosol types (dust, polluted dust, and elevated smoke) at the six sub-regions. It is evident that all MAEC profiles exhibit a similar pattern that the maxima occurred near the ground while gradually decreasing with an increase of height except for different vertical extents and extinction values. For all-aerosol loading,

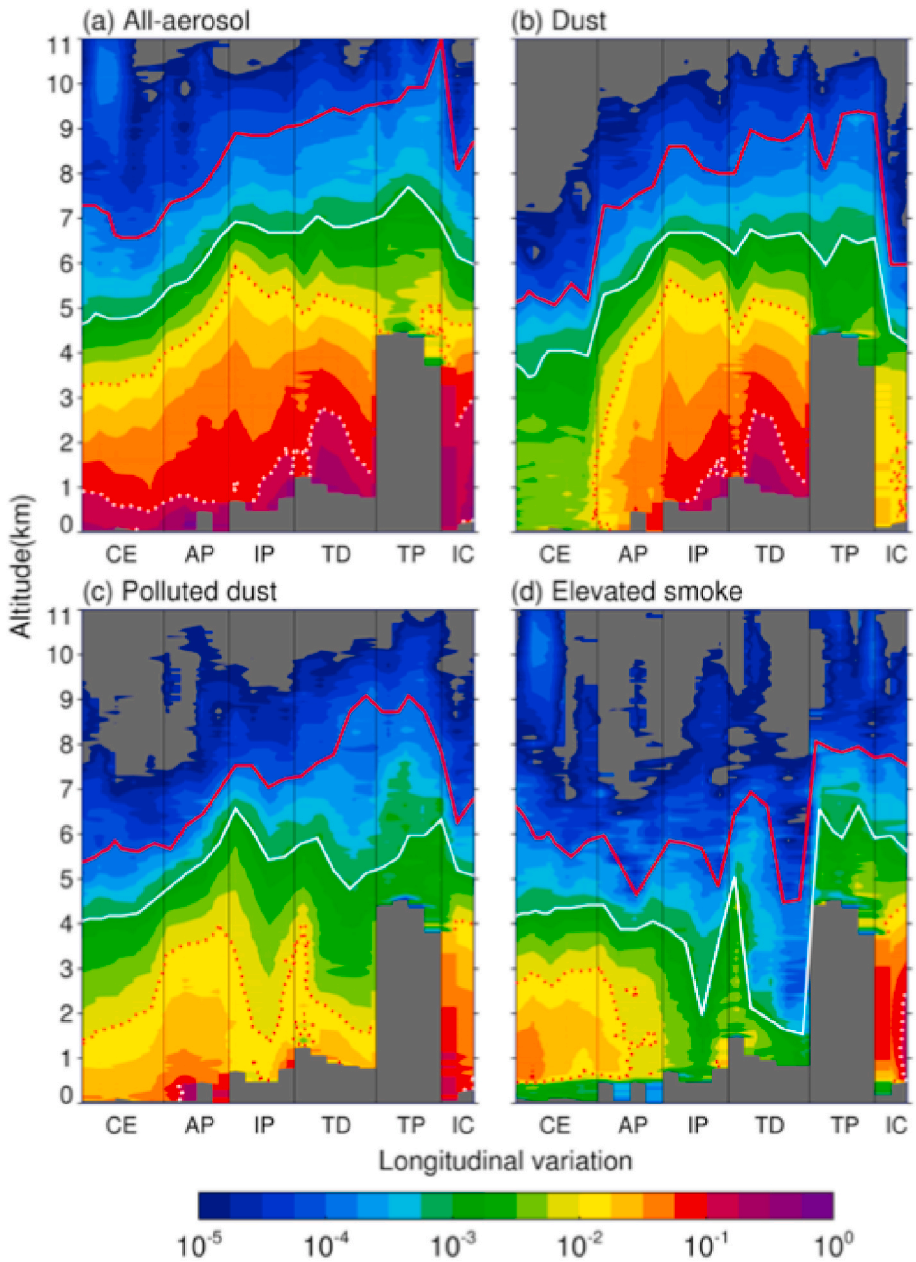

Fig. 5. Longitudinal variation of the decadal MAEC (km^{-1}) for (a) All-aerosol, (b) Dust, (c) Polluted dust, and (d) Elevated smoke over the CE (5–30 °E), the AP (30–50 °E), the IP (50–70 °E), the TD (70–95 °E), the TP (80–100 °E), and the IC (95–105 °E). The red solid line, white solid line, red dotted line and white dotted line indicate the heights where the aerosol extinction equals to 0.0001 (aerosol layer top), 0.001 (low extinction), 0.01(middle extinction), and 0.1 km^{-1} (strong extinction), respectively.

there is no noticeable aerosol concentration (>0.001 km^{-1}) in the atmosphere above 7.5 km. However, it is noteworthy that the heights of aerosol layer top and LE layer increased with the topographic heights in the six sub-regions (refer to Figs. 5a and 6a). The SE, ME, and LE layers for all-aerosol in the TD and the IP showed a consistent pattern with those for dust as shown in Fig. 5a and b, indicating that the columnar AODs in the TD and the IP are mainly dominated by dust particles, accounting for 96% and 86% of total extinction respectively. As the total extinction in the AP, the CE and the IC is dependent on the distinct dominating aerosol types, however, the SE, ME and LE layers for dust (Fig. 5b), polluted dust (Fig. 5c) and elevated smoke (Fig. 5d) differed from those for all-aerosol (Fig. 5a). In the AP, the contribution of polluted dust extinction (38%) is slightly higher than those of dust (31%) and elevated smoke (12%). However, it was found that the elevated smokes were concentrated on higher altitudes above the ground with a strong vertical extent in the CE and the IC. In addition, the extinction (contribution) of the elevated smoke in the CE and the IC was up to 0.06 (32%) and 0.12 (28%) respectively. In section 4.2, this study found that the indistinguishable polluted continental/smoke trapped within the PBL accounted for about 42% and 30% in the CE and the IC as listed in Table 2. Such a result indicates that the CE is mainly dominated by the polluted continental/smoke and the elevated smoke while the contributions of the polluted dust, the elevated smoke and the polluted continental/smoke are dominant in the IC. The columnar AODs in the IC were about 2–3 times as much as in CE.

Fig. 6 shows the latitudinal variation of the decadal MAEC profile for only the TD, the TP, and the IC due to spanning about 20 latitudes in the whole PTP. The SE signal layer in the IC was obviously trapped mostly below 2.8 km a.m.s.l. while the latitude increased and elevated up to 3.5 km a.m.s.l. at the junction between the TP and the IC. Likewise, at the transition between TD and TP, the altitudes of the SE signals layer also increased gradually from north to south. Although the rough spatial grid of CL3AP products contains large amounts of aerosols in the nearby PTP, it is an indisputable fact that the altitude of the SE signals was elevated as the altitude increased toward the TP. Undoubtedly, the TP is a subregion with the strongest vertical transport in the PTP region and the

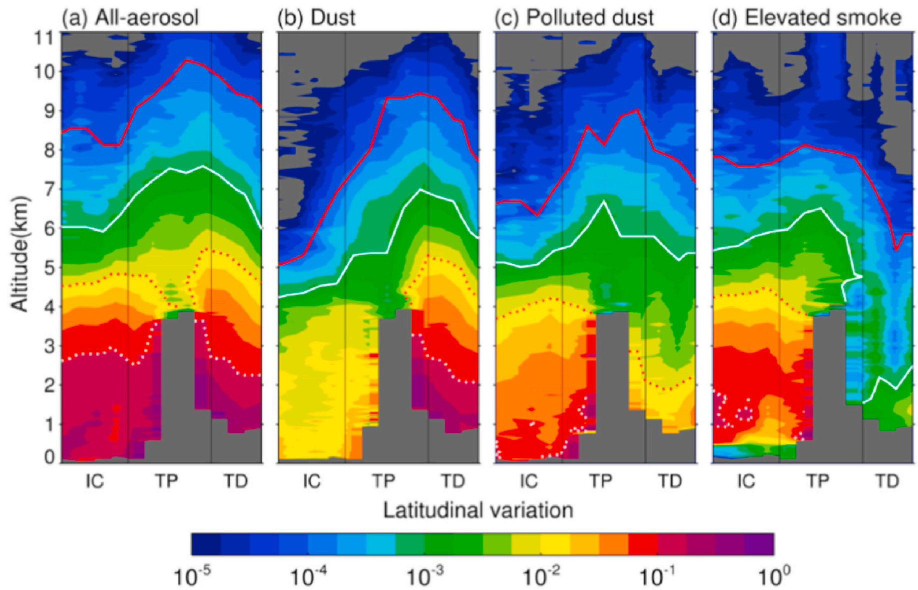

Fig. 6. Latitudinal variation of the decadal MAEC (km^{-1}) for (a) All-aerosol, (b) Dust, (c) Polluted dust, and (d) Elevated smoke over the IC (19–27 ^{o}N), the TP (27–37 ^{o}N), and the TD (37–43 ^{o}N) sub-regions.

Table 2
The annual mean AODs and relative contribution of the dominating aerosol observed by CALIOP over six sub-regions of the PTP.

Aerosol types	Sub-regions of the PTP					
	CE	AP	IP	TD	TP	IC
All-aerosol	0.19	0.26	0.253	0.453	0.012	0.43
Dust	0.01 (5%)	0.08 (31%)	0.218 (86%)	0.439 (96%)	0.005 (42%)	0.04 (9%)
Polluted dust	0.04 (21%)	0.10 (38%)	0.029 (12%)	0.012 (2.6%)	0.004 (33%)	0.14 (33%)
Elevated smoke	0.06 (32%)	0.03 (12%)	0.006 (2%)	0.002 (0.4%)	0.003 (25%)	0.12 (28%)
Others[a]	0.08 (42%)	0.05 (19%)	–	–	–	0.13 (30%)

[a] Represents the estimated value of other aerosols.

LE signal layer was up to 7.5 km a.m.s.l. and the maximum altitude of the aerosol layer top exceeded 10 km a.m.s.l. These results indicate that important natural and anthropogenic aerosols sourced from the nearby PTP are converged to the TP. Besides, the vertical transport induced by Asian monsoon and the heat source, i.e., the 'elevated heat pump' effect, could not only trigger strong convergence but also induce the vertical transport of aerosols from neighboring sources (Lau et al., 2006, 2018; Li et al., 2016b, 2019; Zhao et al., 2020).

It is interesting to note that the occurrence of polluted dust always accompanied by dust or smoke aerosol as shown in the longitudinal or latitudinal distributions of the MAEC profile. Furthermore, it was observed that the maxima of MAEC for dust and polluted dust occurred near the surface and gradually decreased with the increase of height. In contrast, the maxima of MAEC for smoke occurred at the height of 0.5–3 km above the ground. These results may be caused by two possible reasons. Firstly, the extinction retrieval of smoke in CL3AP is derived from only the elevated smoke aerosol. In other words, the polluted continental/smoke that is trapped in the PBL is neglected. Secondly, the smoke plume can be injected into the higher atmosphere due to combustion buoyancy, as discussed by Kahn et al. (2008) and Remy et al. (2017).

4.4. Trends for the dominating aerosol types

Using the linear regression approach, this study examined the decadal AOD trends for the dominating aerosol types to better understand the changes of aerosol loading and to assess their effects on future changes of climate over the PTP region. Especially, this study paid attention to the seasonal AOD trends not only to avoid insignificant annual trends driven by opposite signals from different seasons but also to evaluate the seasonal trends for the dominating aerosol types. Employing the AOD anomalies for each sub-region, the least square fit was applied to detect the seasonal AOD trends based on a method proposed by Weatherhead et al. (1998). In addition, the statistical significance of the estimated trend was confirmed by the student's *t-test*. Fig. 7 presents the decadal trends for all-aerosol and the dominating aerosol types at six sub-regions during the four seasons, where the hatched bars represent the statistically significant trend at $\geq$ 90% significance level. Overall, there are distinct seasonal and regional features in the decadal AOD trends of aerosol loading.

The IC, mainly affected by human activities and dominated by the mixture of polluted dust, elevated smoke and polluted continental/smoke, showed the strongest seasonal trends (upward and downward) among the sub-regions in the PTP. As a whole, the decadal trend of all-aerosol columnar AOD was consistent with that of the dominating aerosol types for each season, indicating that the emissions from local industrial and anthropogenic pollutants are mainly contributed to these tendencies. Except for MAM, the total aerosol loading showed the statistically significant downward trends in response to a significant decrease in the corresponding dominating aerosol types, e.g., the dust transported from the India subcontinent in JJA, the elevated smoke and the polluted dust in SON, and the polluted dust in DJF. Similar downward trends of AOD in JJA, SON and DJF over the IC region were observed in the study by Kang et al. (2017), which based on the OMI satellite retrievals for the period of 2005–2016. However, the columnar AOD in MAM showed a significant and strong upward trend caused by the elevated smoke injected above the PBL from local forest fires. The upward trends for AOD driven by smoke may correspond to an increase in fires, driven by extreme heat waves, in southeast Asia particularly over the last few years (Fernandes et al., 2017; Huijnen et al., 2016).

Of the second cleanest sub-region after the TP, the all-aerosol columnar AOD in the CE totally showed the insignificant AOD trends except for in DJF. The total aerosol loading in DJF showed a significant

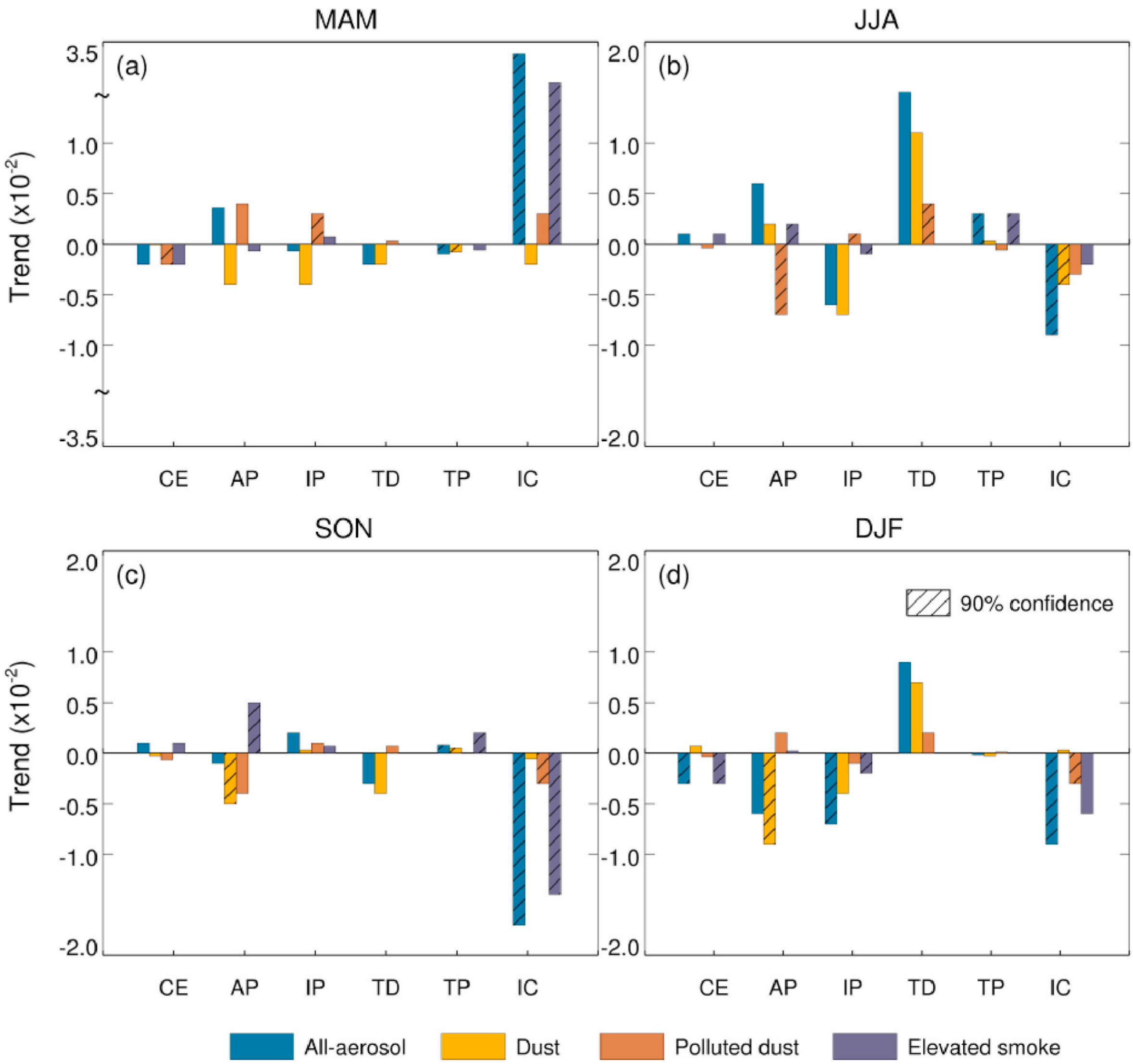

Fig. 7. The linear trends (unit: year^{-1}) of AOD for (a) All-aerosol, (b) Dust, (c) Polluted dust, and (d) Elevated smoke over six sub-regions of the PTP during 2007–2016. The hatched bars represent the statistically significant trend at larger than 90% significance level.

downward trend, which is consistent with the previous studies via AERONET and satellite measurements (Che et al., 2019a; Hsu et al., 2012; Yoon et al., 2014). In addition, the significant decreasing trend for AOD is mainly attributed to the reduction of elevated smoke mainly driven by environmental regulations over the last decades. Moreover, a significant downward trend in MAM for the polluted dust, dominating aerosol type, does not have a significant impact on a decreasing AOD trend for total aerosol loading.

Total aerosol loading in the AP showed a downward trend during SON and DJF while an increasing trend during MAM and JJA. However, the upward and downward trends were statistically insignificant, which may be closely related to the opposite contribution between the Sahara dust transport and the emissions of local industrial and anthropogenic pollutants. The dust particles in Africa had decreased significantly over the last decade due to still surface winds over dust source regions in North Africa (Evan et al., 2016). Thus, the downward AOD trends of dust transported to the AP, statistically significant in SON and DJF, were observed for all seasons except for JJA. In contrast, an increasing AOD trend for the elevated smoke was also observed during JJA and SON, caused by the emissions of local industrial and anthropogenic pollutants. Therefore, the insignificant trends for total aerosol loading during JJA and SON are mainly driven by the offset effect between a decreasing trend for the dust or the polluted dust and an increasing trend for the elevated smoke.

The trends for total aerosol loading in the IP are mainly dependent on the joint effect of Middle East dust transport and local dust emissions (Givehchi et al., 2013). Thus, the dust and the polluted dust, the typical dominating aerosol types, mainly dominate the trend of total aerosol loading. A decreasing trend for the dust was found for all seasons except for SON, which is also consistent with a recent study about the trend of Middle East dust over the last decade although these decreasing trends were statistically insignificant (Mehta et al., 2018). The IP showed a statistically significant downward trend for total aerosol loading during DJF, which is mainly driven by a significant decrease in the elevated smoke. Besides, insignificant trends of total aerosol loading in MAM and JJA are mainly driven by an offset effect between changes in the polluted dust and dust.

Contrary to the IP, the trend for total aerosol loading in the TD was completely driven by local dust emissions. A decreasing trend in MAM and SON was observed while an increasing trend in JJA and DJF, despite statistically insignificant. Previous studies suggested a decreasing frequency of dust based on a TD index, which is likely caused by the Arctic amplification (Liu et al., 2020) and an enhanced geopotential height in the Mongolian plateau and the middle Siberian region (Wang et al., 2008). It is noteworthy that the previous studies had examined a long-term trend of frequency regardless seasonal variability in the decadal AOD trends. The increasing trend needs to be further investigated to assess the effects of the rising near-surface temperatures on the decadal AOD trends as in the previous studies in Africa (Camberlin, 2017; Engelbrecht et al., 2015).

As mentioned earlier, the TP has been regularly exposed to polluted air masses with significant amounts of absorbing aerosols while it was identified as the cleanest region in the PTP in this study. Total aerosol loading showed a significant increasing trend in JJA and SON while a significant decreasing trend in MAM. These significant trends are driven by an increase in the elevated smoke in JJA and SON and a decrease in the dust in response to long-range transport and local emissions from desertification and human activities such as overgrazing, intensive biomass burning and tourism development over recent years (Li et al., 2016a). It is evident that these increasing absorbing aerosols floating in the atmosphere may further enhance the snow-darkening effect and the potential risk of snow-melt and glacier retreat in the future.

5. Conclusions

Employing the 10-year (2007–2016) active and passive aerosol products derived from CALIOP, MODIS and OMI sensors of A-Train constellation, this study investigated the columnar and vertical distributions of optical properties, the dominating aerosol types, and their decadal trends in the PTP that consists of the six sub-regions defined by the distinct climatic features and the potential natural and anthropogenic aerosol sources. The results showed:

- The distributions of columnar AOD in the PTP varied with the sub-regions and seasons. Among the six sub-regions, the TP was the cleanest one with the smallest columnar AOD. Due to high uncertainty in the columnar AODs, however, an advanced measurement may be necessary to better understand the spatial distribution of aerosols in the PTP region.
- The whole PTP region was mainly dominated by dust, polluted dust and elevated smoke. In particular, dust particles accounted for 96% and 86% of total extinction in the TD and the IP, respectively.
- This study also found a strong vertical transport at higher altitude (above 10 km a.m.s.l.) in the TD during MAM. Polluted dust always accompanied by dust aerosol or smoke mainly caused by biomass burning. In addition, the AP, the IC, and the CE were affected by the mixture of the dominated aerosol types.
- The MAEC showed an obvious variability at the sub-regions with a tendency that it decreased as the topographic height increased. Without a noticeable aerosol concentration (>0.001 km^{-1}) above 7.5 km a.m.s.l., the height of the aerosol layer top and LE layer totally increased with the topographic height of the six sub-regions. The TP was a sub-region with the strongest vertical transport, indicating that the natural and anthropogenic aerosols from both the PTP and surroundings are converged strongly into higher altitudes driven by the Asian monsoon and the 'elevated heat pump' effect.
- From a decadal AOD trend analysis at a seasonal scale, this study found that the decadal AOD trend corresponded to the contributions of dominating aerosol types at the sub-regions. In particular, the largest upward trend was found in the IC during MAM, which may be caused by the elevated smoke from local industrial and anthropogenic pollutants.
- Although the TD showed inconsistent trends with previous studies, this study found that the TP has been regularly exposed to polluted air masses with significant amounts of absorbing aerosols. Consequently, these increasing absorbing aerosol floating in the atmosphere may influence on enhancing the snow-darkening effect and the potential risk of snow-melt and glacier retreat in the future. Furthermore, the above understandings are of great significance for assessing their effects on the retreat of glaciers, increase of lake levels, river runoff, and the regional and even global hydrologic cycle.

Declaration of competing interest

The authors declare that they have no known competing financial interests or personal relationships that could have appeared to influence the work reported in this paper.

CRediT authorship contribution statement

Tianhe Wang: Conceptualization, Methodology, Writing - original draft, Writing - review & editing. **Yixuan Chen:** Data curation, Software, Visualization, Formal analysis. **Zewen Gan:** Formal analysis. **Ying Han:** Data curation. **Jiming Li:** Formal analysis. **Jianping Huang:** Supervision, Conceptualization, Writing - review & editing.

Acknowledgments

This research was funded by the Srategic Priority Research Program, Chinese Academy of Sciences (XDA20060103) and the National Natrual Science Foundataion of China (41775022, 41521004, 41430425). The authors gratefully acknowledge the data support from NASA for making satellite datasets accessible in public. CALIPSO data were processed from the NASA Langley Research Center Atmospheric Science Data Center (http://eosweb.larc.nasa.gov/). MODIS and OMI data were acquired from the NASA Giovanni online data system (https://giovanni.gsfc.nasa.gov/giovanni/), developed and maintained by the NASA GES DISC.

References

Ackerman, A.S., Toon, O.B., Stevens, D.E., Heymsfield, A.J., Ramanathan, V., Welton, E. J., 2000. Reduction of tropical cloudiness by soot. Science 288, 1042–1047.
Alfaro-Contreras, R., Zhang, J.L., Reid, J.S., Christopher, S., 2017. A study of 15-year aerosol optical thickness and direct shortwave aerosol radiative effect trends using MODIS, MISR, CALIOP and CERES. Atmos. Chem. Phys. 17, 13849–13868.
Amiridis, V., Giannakaki, E., Balis, D., Gerasopoulos, E., Pytharoulis, I., Zanis, P., Kazadzis, S., Melas, D., Zerefos, C.S., 2010. Smoke injection heights from agricultural burning in Eastern Europe as seen by CALIPSO. Atmos. Chem. Phys. 10, 11567–11576.
Badarinath, K.V.S., Kharol, S.K., Kaskaoutis, D.G., Sharma, A.R., Ramaswamy, V., Kambezidis, H.D., 2010. Long-range transport of dust aerosols over the Arabian Sea and Indian region A case study using satellite data and ground-based measurements. Global Planet. Change 72, 164–181.
Barnett, T.P., Adam, J.C., Lettenmaier, D.P., 2005. Potential impacts of a warming climate on water availability in snow-dominated regions. Nature 438, 303–309.
Bayat, A., Masoumi, A., Khalesifard, H.R., 2011. Retrieval of atmospheric optical parameters from ground-based sun-photometer measurements for Zanjan, Iran. Atmos.Measur. Tech. 4, 857–863.
Camberlin, P., 2017. Temperature trends and variability in the Greater Horn of Africa: interactions with precipitation. Clim. Dynam. 48, 477–498.
Cao, G., Zhang, X., Wang, Y., Zheng, F., 2008. Estimation of emissions from field burning of crop straw in China. Chin. Sci. Bull. 53, 784–790.
Che, H., Gui, K., Xia, X., Wang, Y., Holben, B.N., Goloub, P., Cuevasagullo, E., Wang, H., Zheng, Y., Zhao, H., 2019a. Large contribution of meteorological factors to inter-decadal changes in regional aerosol optical depth. Atmos. Chem. Phys. 19, 10497–10523.
Che, H., Xia, X., Zhao, H., Dubovik, O., Holben, B.N., Goloub, P., Cuevasagullo, E., Estelles, V., Wang, Y., Zhu, J., 2019b. Spatial distribution of aerosol microphysical and optical properties and direct radiative effect from the China Aerosol Remote Sensing Network. Atmos. Chem. Phys. 19, 11843–11864.
Che, H., Zhang, X., Xia, X., Goloub, P., Holben, B.N., Zhao, H., Wang, Y., Zhang, X., Wang, H., Blarel, L., 2015. Ground-based aerosol climatology of China: aerosol optical depths from the China Aerosol Remote Sensing Network (CARSNET) 2002–2013. Atmos. Chem. Phys. 15, 7619–7652.
Chimot, J., Veefkind, J.P., Vlemmix, T., de Haan, J.F., Amiridis, V., Proestakis, E., Marinou, E., Levelt, P.F., 2017. An exploratory study on the aerosol height retrieval from OMI measurements of the 477 nm O2-O2 spectral band using a neural network approach. Atmos.Measur. Tech. 10, 783–809.
Cong, Z., Kawamura, K., Kang, S., Fu, P., 2015. Penetration of biomass-burning emissions from South Asia through the Himalayas: new insights from atmospheric organic acids. Sci. Rep. 5, 9580.
Davidson, C.I., Phalen, R.F., Solomon, P.A., 2005. Airborne particulate matter and human health: a review. Aerosol. Sci. Technol. 39, 737–749.

Deng, Z.Z., Zhao, C.S., Ma, N., Liu, P.F., Ran, L., Xu, W.Y., Chen, J., Liang, Z., Liang, S., Huang, M.Y., Ma, X.C., Zhang, Q., Quan, J.N., Yan, P., Henning, S., Mildenberger, K., Sommerhage, E., Schafer, M., Stratmann, F., Wiedensohler, A., 2011. Size-resolved and bulk activation properties of aerosols in the North China Plain. Atmos. Chem. Phys. 11, 3835–3846.
Engelbrecht, F., Adegoke, J., Bopape, M.M., Naidoo, M., Garland, R.M., Thatcher, M., Mcgregor, J.L., Katzfey, J., Werner, M., Ichoku, C., 2015. Projections of rapidly rising surface temperatures over Africa under low mitigation. Environ. Res. Lett. 10, 085004.
Evan, A.T., Flamant, C., Gaetani, M., Guichard, F., 2016. The past, present and future of African dust. Nature 531, 493–495.
Fan, H., Zhao, C., Yang, Y., 2020. A comprehensive analysis of the spatio-temporal variation of urban air pollution in China during 2014–2018. Atmos. Environ. 220, 117066.
Fernandes, K., Verchot, L.V., Baethgen, W.E., Gutierrezvelez, V.H., Pinedovasquez, M., Martius, C., 2017. Heightened fire probability in Indonesia in non-drought conditions: the effect of increasing temperatures. Environ. Res. Lett. 12, 054002.
Garrett, T.J., Zhao, C., 2006. Increased Arctic cloud longwave emissivity associated with pollution from mid-latitudes. Nature 440, 787–789.
Gautam, R., Hsu, N.C., Lau, W.K.M., Yasunari, T.J., 2013. Satellite observations of desert dust-induced Himalayan snow darkening. Geophys. Res. Lett. 40, 988–993.
Ge, J., Huang, J., Xu, C.P., Qi, Y.L., Liu, H., 2014. Characteristics of Taklimakan dust emission and distribution: a satellite and reanalysis field perspective. J. Geophys. Res.: Atmos. 119, 11772–11783.
Givehchi, R., Arhami, M., Tajrishy, M., 2013. Contribution of the Middle Eastern dust source areas to PM10 levels in urban receptors: case study of Tehran, Iran. Atmos. Environ. 75, 287–295.
Gul, C., Puppala, S.P., Kang, S., Adhikary, B., Zhang, Y., Ali, S., Li, Y., Li, X., 2018. Concentrations and source regions of light-absorbing particles in snow/ice in northern Pakistan and their impact on snow albedo. Atmos. Chem. Phys. 18, 4981–5000.
Hofer, J., Althausen, D., Abdullaev, S.F., Makhmudov, A.N., Nazarov, B.I., Schettler, G., Engelmann, R., Baars, H., Fomba, K.W., Mueller, K., Heinold, B., Kandler, K., Ansmann, A., 2017. Long-term profiling of mineral dust and pollution aerosol with multiwavelength polarization Raman lidar at the Central Asian site of Dushanbe, Tajikistan: case studies. Atmos. Chem. Phys. 17, 14559–14577.
Hsu, N.C., Gautam, R., Sayer, A.M., Bettenhausen, C., Li, C., Jeong, M.J., Tsay, S.C., Holben, B.N., 2012. Global and regional trends of aerosol optical depth over land and ocean using SeaWiFS measurements from 1997 to 2010. Atmos. Chem. Phys. 12, 8037–8053.
Hsu, N.C., Jeong, M.J., Bettenhausen, C., Sayer, A.M., Hansell, R., Seftor, C.S., Huang, J., Tsay, S.C., 2013. Enhanced Deep Blue aerosol retrieval algorithm: the second generation. J. Geophys. Res.: Atmos. 118, 9296–9315.
Huang, J., Guan, X., Ji, F., 2012. Enhanced cold-season warming in semi-arid regions. Atmos. Chem. Phys. 12, 5391–5398.
Huang, J., Ji, M., Xie, Y., Wang, S., He, Y., Ran, J., 2015a. Global semi-arid climate change over last 60 years. Clim. Dynam. 46, 1131–1150.
Huang, J., Lin, B., Minnis, P., Wang, T., Wang, X., Hu, Y., Yi, Y., Ayers, J.K., 2006a. Satellite-based assessment of possible dust aerosols semi-direct effect on cloud water path over East Asia. Geophys. Res. Lett. 33, L19802.
Huang, J., Liu, J., Chen, B., Nasiri, S., 2015b. Detection of anthropogenic dust using CALIPSO lidar measurements. Atmos. Chem. Phys. 15, 11653–11665.
Huang, J., Minnis, P., Chen, B., Huang, Z., Liu, Z., Zhao, Q., Yi, Y., Ayers, J.K., 2008. Long-range transport and vertical structure of Asian dust from CALIPSO and surface measurements during PACDEX. J. Geophys. Res.: Atmos. 113, D23212.
Huang, J., Minnis, P., Lin, B., Wang, T., Yi, Y., Hu, Y., Sunmack, S., Ayers, K., 2006b. Possible influences of Asian dust aerosols on cloud properties and radiative forcing observed from MODIS and CERES. Geophys. Res. Lett. 33, L06824.
Huang, J., Minnis, P., Yi, Y., Tang, Q., Wang, X., Hu, Y., Liu, Z., Ayers, K., Trepte, C., Winker, D., 2007. Summer dust aerosols detected from CALIPSO over the Tibetan Plateau. Geophys. Res. Lett. 34, L18805.
Huang, J., Wang, T., Wang, W., Li, Z., Yan, H., 2014. Climate effects of dust aerosols over East Asian arid and semiarid regions. J. Geophys. Res.: Atmos. 119, 11398–11416.
Huang, J., Yu, H., Dai, A., Wei, Y., Kang, L., 2017. Drylands face potential threat under 2 °C global warming target. Nat. Clim. Change 7, 417–422.
Huang, J., Yu, H., Guan, X., Wang, G., Guo, R., 2015c. Accelerated dryland expansion under climate change. Nat. Clim. Change 6, 166–171.
Huang, Z., Huang, J., Hayasaka, T., Wang, S., Zhou, T., Jin, H., 2015d. Short-cut transport path for Asian dust directly to the Arctic: a case study. Environ. Res. Lett. 10, 114018.
Huijnen, V., Wooster, M.J., Kaiser, J.W., Gaveau, D.L.A., Flemming, J., Parrington, M., Inness, A., Murdiyarso, D., Main, B., van Weele, M., 2016. Fire carbon emissions over maritime southeast Asia in 2015 largest since 1997. Sci. Rep. 6, 26886.
Israelevich, P., Ganor, E., Alpert, P., Kishcha, P., Stupp, A., 2012. Predominant transport paths of saharan dust over the mediterranean Sea to Europe. J. Geophys. Res.: Atmos. 117, D02205.
Jacobi, H.W., Lim, S., Menegoz, M., Ginot, P., Laj, P., Bonasoni, P., Stocchi, P., Marinoni, A., Arnaud, Y., 2015. Black carbon in snow in the upper Himalayan Khumbu Valley, Nepal: observations and modeling of the impact on snow albedo, melting, and radiative forcing. Cryosphere 9, 1685–1699.
Jin, Q., Wang, C., 2018. The greening of Northwest Indian subcontinent and reduction of dust abundance resulting from Indian summer monsoon revival. Sci. Rep. 8, 1–9.
Kabatas, B., Unal, A., Pierce, R.B., Kindap, T., Pozzoli, L., 2014. The contribution of Saharan dust in PM10 concentration levels in Anatolian Peninsula of Turkey. Sci. Total Environ. 488, 413–421.
Kahn, R.A., Chen, Y., Nelson, D.L., Leung, F.-Y., Li, Q., Diner, D.J., Logan, J.A., 2008. Wildfire smoke injection heights: two perspectives from space. Geophys. Res. Lett. 35, L04809.
Kang, L., Chen, S., Huang, J., Zhao, S., Ma, X., Yuan, T., Zhang, X., Xie, T., 2017. The spatial and temporal distributions of absorbing aerosols over east Asia. Rem. Sens. 9, 1050.
Kang, S., Xu, Y., You, Q., Fluegel, W.-A., Pepin, N., Yao, T., 2010. Review of climate and cryospheric change in the Tibetan Plateau. Environ. Res. Lett. 5, 015101.
Kim, M., Kim, S.W., Yoon, S., Omar, A., 2013. Comparison of aerosol optical depth between CALIOP and MODIS-Aqua for CALIOP aerosol subtypes over the ocean. J. Geophys. Res.: Atmos. 118, 13241–13252.
Kocak, M., Theodosi, C., Zarmpas, P., Seguret, M.J.M., Herut, B., Kallos, G., Mihalopoulos, N., Kubilay, N., Nimmo, M., 2012. Influence of mineral dust transport on the chemical composition and physical properties of the Eastern Mediterranean aerosol. Atmos. Environ. 57, 266–277.
Koren, I., Kaufman, Y.J., Remer, L.A., Martins, J.V., 2004. Measurement of the effect of Amazon smoke on inhibition of cloud formation. Science 303, 1342–1345.
Kubilay, N., Nickovic, S., Moulin, C., Dulac, F., 2000. An illustration of the transport and deposition of mineral dust onto the eastern Mediterranean. Atmos. Environ. 34, 1293–1303.
Lau, K.M., Kim, M.K., Kim, K.M., 2006. Asian summer monsoon anomalies induced by aerosol direct forcing: the role of the Tibetan Plateau. Clim. Dynam. 26, 855–864.
Lau, W.K.M., Kim, M.-K., Kim, K.-M., Lee, W.-S., 2010. Enhanced surface warming and accelerated snow melt in the Himalayas and Tibetan Plateau induced by absorbing aerosols. Environ. Res. Lett. 5, 025204.
Lau, W.K.M., Yuan, C., Li, Z., 2018. Origin, maintenance and variability of the asian tropopause aerosol layer (ATAL): the roles of monsoon dynamics. Sci. Rep. 8, 3960.
Léon, J.-F., Legrand, M., 2003. Mineral dust sources in the surroundings of the north Indian Ocean. Geophys. Res. Lett. 30, 1309.
Levy, R.C., Mattoo, S., Munchak, L.A., Remer, L.A., Sayer, A.M., Patadia, F., Hsu, N.C., 2013. The Collection 6 MODIS aerosol products over land and ocean. Atmos.Measur. Tech. 6, 2989–3034.
Li, C., Bosch, C., Kang, S., Andersson, A., Chen, P., Zhang, Q., Cong, Z., Chen, B., Qin, D., Gustafsson, O., 2016a. Sources of black carbon to the Himalayan-Tibetan Plateau glaciers. Nat. Commun. 7, 12574.
Li, J., Carlson, B.E., Dubovik, O., Lacis, A.A., 2014. Recent trends in aerosol optical properties derived from AERONET measurements. Atmos. Chem. Phys. 14, 12271–12289.
Li, Z., Lau, W.K.M., Ramanathan, V., Wu, G., Ding, Y., Manoj, M., Liu, J., Qian, Y., Li, J., Zhou, T., 2016b. Aerosol and monsoon climate interactions over Asia. Rev. Geophys. 54, 866–929.
Li, Z., Niu, F., Fan, J., Liu, Y., Rosenfeld, D., Ding, Y., 2011. Long-term impacts of aerosols on the vertical development of clouds and precipitation. Nat. Geosci. 4, 888–894.
Li, Z., Wang, Y., Guo, J., Zhao, C., Cribb, M., Dong, X., Fan, J., Gong, D., Huang, J., Jiang, M., 2019. East Asian study of tropospheric aerosols and their impact on regional clouds, precipitation, and climate (EAST-AIRCPC). J. Geophys. Res.: Atmos. 124, 13026–13054.
Liu, D., Wang, Z., Liu, Z., Winker, D.M., Trepte, C.R., 2008. A height resolved global view of dust aerosols from the first year CALIPSO lidar measurements. J. Geophys. Res.: Atmos. 113, D16214.
Liu, J., Wu, D., Liu, G., Mao, R., Chen, S., Ji, M., Fu, P., Sun, Y., Pan, X., Jin, H., 2020. Impact of Arctic amplification on declining spring dust events in East Asia. Clim. Dynam. 54, 1913–1935.
Liu, Z., Vaughan, M.A., Winker, D.M., Hostetler, C.A., Poole, L.R., Hlavka, D.L., Hart, W. K., Mcgill, M.J., 2004. Use of probability distribution functions for discriminating between cloud and aerosol in lidar backscatter data. J. Geophys. Res.: Atmos. 109, D15202.
Luo, T., Wang, Z., Zhang, D., Liu, X., Wang, Y., Yuan, R., 2015. Global dust distribution from improved thin dust layer detection using A-train satellite lidar observations. Geophys. Res. Lett. 42, 620–628.
Luo, Y., Zheng, X., Zhao, T., Chen, J., 2014. A climatology of aerosol optical depth over China from recent 10 years of MODIS remote sensing data. Int. J. Climatol. 34, 863–870.
Luthi, Z.L., Skerlak, B., Kim, S.W., Lauer, A., Mues, A., Rupakheti, M., Kang, S., 2015. Atmospheric brown clouds reach the Tibetan Plateau by crossing the Himalayas. Atmos. Chem. Phys. 15, 6007–6021.
Mckendry, I.G., Strawbridge, K.B., Oneill, N.T., Macdonald, A.M., Liu, P.S.K., Leaitch, W. R., Anlauf, K.G., Jaegle, L., Fairlie, T.D., Westphal, D.L., 2007. Trans-Pacific transport of Saharan dust to western North America: a case study. J. Geophys. Res.: Atmos. 112, D01103.
Mehta, M., Singh, N., Anshumali, 2018. Global trends of columnar and vertically distributed properties of aerosols with emphasis on dust, polluted dust and smoke - inferences from 10-year long CALIOP observations. Remote Sens. Environ. 208, 120–132.
Mehta, M., Singh, R., Singh, A., Singh, N., Anshumali, 2016. Recent global aerosol optical depth variations and trends - a comparative study using MODIS and MISR level 3 datasets. Remote Sens. Environ. 181, 137–150.
Menon, S., Hansen, J., Nazarenko, L., Luo, Y., 2002. Climate effects of black carbon aerosols in China and India. Science 297, 2250–2253.
Mona, L., Pappalardo, G., Amodeo, A., D'Amico, G., Madonna, F., Boselli, A., Giunta, A., Russo, F., Cuomo, V., 2009. One year of CNR-IMAA multi-wavelength Raman lidar measurements in coincidence with CALIPSO overpasses: level 1 products comparison. Atmos. Chem. Phys. 9, 7213–7228.
Omar, A.H., Winker, D.M., Kittaka, C., Vaughan, M.A., Liu, Z., Hu, Y., Trepte, C.R., Rogers, R.R., Ferrare, R.A., Lee, K.-P., Kuehn, R.E., Hostetler, C.A., 2009. The

CALIPSO automated aerosol classification and lidar ratio selection algorithm. J. Atmos. Ocean. Technol. 26, 1994–2014.
Papagiannopoulos, N., Mona, L., Alados-Arboledas, L., Amiridis, V., Baars, H., Binietoglou, I., Bortoli, D., D'Amico, G., Giunta, A., Luis Guerrero-Rascado, J., Schwarz, A., Pereira, S., Spinelli, N., Wandinger, U., Wang, X., Pappalardo, G., 2016. CALIPSO climatological products: evaluation and suggestions from EARLINET. Atmos. Chem. Phys. 16, 2341–2357.
Penning de Vries, M.J.M., Beirle, S., Hormann, C., Kaiser, J.W., Stammes, P., Tilstra, L.G., Tuinder, O.N.E., Wagner, T., 2015. A global aerosol classification algorithm incorporating multiple satellite data sets of aerosol and trace gas abundances. Atmos. Chem. Phys. 15, 10597–10618.
Pokharel, M., Guang, J., Liu, B., Kang, S., Ma, Y., Holben, B.N., Xia, X.a., Xin, J., Ram, K., Rupakheti, D., Wan, X., Wu, G., Bhattarai, H., Zhao, C., Cong, Z., 2019. Aerosol properties over Tibetan plateau from a decade of AERONET measurements: baseline, types, and influencing factors. J. Geophys. Res.: Atmos. 124, 13357–13374.
Prospero, J.M., Ginoux, P., Torres, O., Nicholson, S.E., Gill, T.E., 2002. Environmental characterization of global sources of atmospheric soil dust identified with the Nimbus 7 Total Ozone Mapping Spectrometer (TOMS) absorbing aerosol product. Rev. Geophys. 40 (1), 2-1-2-31.
Ramanathan, V., Crutzen, P.J., Kiehl, J.T., Rosenfeld, D., 2001. Aerosols, climate, and the hydrological cycle. Science 294, 2119–2124.
Ramanathan, V., Ramana, M.V., Roberts, G., Kim, D., Corrigan, C., Chung, C., Winker, D., 2007. Warming trends in Asia amplified by brown cloud solar absorption. Nature 448, 575–578.
Rashki, A., Kaskaoutis, D.G., Eriksson, P.G., Rautenbach, C.J.d.W., Flamant, C., Vishkaee, F.A., 2014. Spatio-temporal variability of dust aerosols over the Sistan region in Iran based on satellite observations. Nat. Hazards 71, 563–585.
Remy, S., Veira, A., Paugam, R., Sofiev, M., Kaiser, J.W., Marenco, F., Burton, S.P., Benedetti, A., Engelen, R.J., Ferrare, R., Hair, J.W., 2017. Two global data sets of daily fire emission injection heights since 2003. Atmos. Chem. Phys. 17, 2921–2942.
Rosenfeld, D., Lohmann, U., Raga, G.B., O'Dowd, C.D., Kulmala, M., Fuzzi, S., Reissell, A., Andreae, M.O., 2008. Flood or drought: how do aerosols affect precipitation? Science 321, 1309–1313.
Savtchenko, A., Ouzounov, D., Ahmad, S., Acker, J., Leptoukh, G., Koziana, J., Nickless, D., 2004. Terra and aqua MODIS products available from NASA GES DAAC. Adv. Space Res. 34, 710–714.
Sayer, A.M., Munchak, L.A., Hsu, N.C., Levy, R.C., Bettenhausen, C., Jeong, M.J., 2014. MODIS Collection 6 aerosol products: comparison between Aqua's e-Deep Blue, Dark Target, and "merged" data sets, and usage recommendations. J. Geophys. Res.: Atmos. 119, 13965–13989.
Schuster, G.L., Vaughan, M., MacDonnell, D., Su, W., Winker, D., Dubovik, O., Lapyonok, T., Trepte, C., 2012. Comparison of CALIPSO aerosol optical depth retrievals to AERONET measurements, and a climatology for the lidar ratio of dust. Atmos. Chem. Phys. 12, 7431–7452.
Sun, W., Liu, Z., Videen, G., Fu, Q., Muinonen, K., Winker, D.M., Lukashin, C., Jin, Z., Lin, B., Huang, J., 2013. For the depolarization of linearly polarized light by smoke particles. J. Quant. Spectrosc. Radiat. Transf. 122, 233–237.
Tanaka, T.Y., Kurosaki, Y., Chiba, M., Matsumura, T., Nagai, T., Yamazaki, A., Uchiyama, A., Tsunematsu, N., Kai, K., 2005. Possible transcontinental dust transport from north Africa and the Middle East to east Asia. Atmos. Environ. 39, 3901–3909.
Tao, M., Chen, L., Wang, Z., Tao, J., Che, H., Wang, X., Wang, Y., 2015. Comparison and evaluation of the MODIS Collection 6 aerosol data in China. J. Geophys. Res.: Atmos. 120, 6992–7005.
Torres, O., Tanskanen, A., Veihelmann, B., Ahn, C., Braak, R., Bhartia, P.K., Veefkind, P., Levelt, P., 2007. Aerosols and surface UV products from Ozone Monitoring Instrument observations: an overview. J. Geophys. Res.: Atmos. 112, D24S47.
Tutsak, E., Kocak, M., 2019. Long-term measurements of aerosol optical and physical properties over the Eastern Mediterranean: hygroscopic nature and source regions. Atmos. Environ. 207, 1–15.
Uno, I., Eguchi, K., Yumimoto, K., Takemura, T., Shimizu, A., Uematsu, M., Liu, Z., Wang, Z., Hara, Y., Sugimoto, N., 2009. Asian dust transported one full circuit around the globe. Nat. Geosci. 2, 557–560.
van Donkelaar, A., Martin, R.V., Brauer, M., Kahn, R., Levy, R., Verduzco, C., Villeneuve, P.J., 2010. Global estimates of ambient fine particulate matter concentrations from satellite-based aerosol optical depth: development and application. Environ. Health Perspect. 118, 847–855.
Wang, T., Huang, J., 2009. A method for estimating optical properties of dusty cloud. Chin. Optic Lett. 7, 368–372.
Wang, X., Huang, J.P., Ji, M.X., Higuchi, K., 2008. Variability of East Asia dust events and their long-term trend. Atmos. Environ. 42, 3156–3165.
Wang, X., Liu, J., Che, H., Ji, F., Liu, J., 2018a. Spatial and temporal evolution of natural and anthropogenic dust events over northern China. Sci. Rep. 8, 2141.
Wang, X., Wen, H., Shi, J., Bi, J., Huang, Z., Zhang, B., Zhou, T., Fu, K., Chen, Q., Xin, J., 2018b. Optical and microphysical properties of natural mineral dust and anthropogenic soil dust near dust source regions over northwestern China. Atmos. Chem. Phys. 18, 2119–2138.
Weatherhead, E.C., Reinsel, G.C., Tiao, G.C., Meng, X.-L., Choi, D., Cheang, W.-K., Keller, T., DeLuisi, J., Wuebbles, D.J., Kerr, J.B., Miller, A.J., Oltmans, S.J., Frederick, J.E., 1998. Factors affecting the detection of trends: statistical considerations and applications to environmental data. J. Geophys. Res.: Atmos. 103, 17149–17161.
Winker, D.M., Tackett, J.L., Getzewich, B.J., Liu, Z., Vaughan, M.A., Rogers, R.R., 2013. The global 3-D distribution of tropospheric aerosols as characterized by CALIOP. Atmos. Chem. Phys. 13, 3345–3361.
Winker, D.M., Vaughan, M.A., Omar, A., Hu, Y., Powell, K.A., Liu, Z., Hunt, W.H., Young, S.A., 2009. Overview of the CALIPSO mission and CALIOP data processing algorithms. J. Atmos. Ocean. Technol. 26, 2310–2323.
Wu, G., Duan, A., Liu, Y., Mao, J., Ren, R., Bao, Q., He, B., Liu, B., Hu, W., 2015. Tibetan Plateau climate dynamics: recent research progress and outlook. Nat. Sci. Rev. 2, 100–116.
Xu, B., Cao, J., Hansen, J., Yao, T., Joswia, D.R., Wang, N., Wu, G., Wang, M., Zhao, H., Yang, W., Liu, X., He, J., 2009. Black soot and the survival of Tibetan glaciers. Proc. Natl. Acad. Sci. U. S. A 106, 22114–22118.
Xu, Y., Ramanathan, V., Washington, W.M., 2016. Observed high-altitude warming and snow cover retreat over Tibet and the Himalayas enhanced by black carbon aerosols. Atmos. Chem. Phys. 16, 1303–1315.
Yan, H., Wang, T., 2020. Ten years of aerosol effects on single-layer overcast clouds over the US southern great plains and the China loess plateau. Adv. Meteorol. 2020, 6719160.
Yang, K., Wu, H., Qin, J., Lin, C., Tang, W., Chen, Y., 2014. Recent climate changes over the Tibetan Plateau and their impacts on energy and water cycle: a review. Global Planet. Change 112, 79–91.
Yang, X., Zhao, C., Guo, J., Wang, Y., 2016. Intensification of aerosol pollution associated with its feedback with surface solar radiation and winds in Beijing. J. Geophys. Res.: Atmos. 121, 4093–4099.
Yang, X., Zhao, C., Zhou, L., Li, Z., Cribb, M., Yang, S., 2018. Wintertime cooling and a potential connection with transported aerosols in Hong Kong during recent decades. Atmos. Res. 211, 52–61.
Yang, Y., Zhao, C., Sun, L., Wei, J., 2019. Improved aerosol retrievals over complex regions using NPP visible infrared imaging radiometer suite observations. Earth Space Sci. 6, 629–645.
Yao, T., Chen, F., Cui, P., Ma, Y., Xu, B., Zhu, L., Zhang, F., Wang, W., Ai, L., Yang, X., 2017. From Tibetan plateau to third Pole and pan-third Pole. Bull. Chin. Acad. Sci. 32, 924–931.
Yao, T.D., Wang, Y.Q., Liu, S.Y., Pu, J.C., Shen, Y.P., Lu, A.X., 2004. Recent glacial retreat in High Asia in China and its impact on water resource in Northwest China. Sci. China Earth Sci. 47, 1065–1075.
Yasunari, T.J., Koster, R.D., Lau, W.K.M., Kim, K., 2015. Impact of snow darkening via dust, black carbon, and organic carbon on boreal spring climate in the Earth system. J. Geophys. Res.: Atmos. 120, 5485–5503.
Yoon, J., Burrows, J.P., Vountas, M., von Hoyningen-Huene, W., Chang, D.Y., Richter, A., Hilboll, A., 2014. Changes in atmospheric aerosol loading retrieved from space-based measurements during the past decade. Atmos. Chem. Phys. 14, 6881–6902.
You, C., Yao, T., Xu, B., Xu, C., Zhao, H., Song, L., 2016. Effects of sources, transport, and postdepositional processes on levoglucosan records in southeastern Tibetan glaciers. J. Geophys. Res.: Atmos. 121, 8701–8711.
Yu, H., Chin, M., Winker, D.M., Omar, A., Liu, Z., Kittaka, C., Diehl, T., 2010. Global view of aerosol vertical distributions from CALIPSO lidar measurements and GOCART simulations: regional and seasonal variations. J. Geophys. Res.: Atmos. 115, D00H30.
Zhang, G., Xie, H., Kang, S., Yi, D., Ackley, S.F., 2011. Monitoring lake level changes on the Tibetan Plateau using ICESat altimetry data (2003-2009). Remote Sens. Environ. 115, 1733–1742.
Zhang, K., Zhao, C., Fan, H., Yang, Y., Sun, Y., 2019. Toward understanding the differences of PM 2.5 characteristics among five China urban cities. Asia-pacific J. Atmos. Sci. 1–10.
Zhang, R., Wang, Y., He, Q., Chen, L., Zhang, Y., Qu, H., Smeltzer, C., Li, J., Alvarado, L. M.A., Vrekoussis, M., Richter, A., Wittrock, F., Burrows, J.P., 2017. Enhanced trans-Himalaya pollution transport to the Tibetan Plateau by cut-off low systems. Atmos. Chem. Phys. 17, 3083–3095.
Zhang, Y.-L., Cao, F., 2015. Fine particulate matter (PM2.5) in China at a city level. Sci. Rep. 5, 14884.
Zhao, C., Garrett, T.J., 2015. Effects of Arctic haze on surface cloud radiative forcing. Geophys. Res. Lett. 42, 557–564.
Zhao, C., Yang, Y., Fan, H., Huang, J., Fu, Y., Zhang, X., Kang, S., Cong, Z., Letu, H., Menenti, M., 2020. Aerosol characteristics and impacts on weather and climate over the Tibetan Plateau. Nat. Sci. Rev. 7, 492–495.